Chapter 14

Nitrogen-Doped Carbon Nanotube/Polymer Nanocomposites Towards Thermoelectric Applications

Mohammad Arjmand and Soheil Sadeghi

Additional information is available at the end of the chapter

http://dx.doi.org/10.5772/65675

Abstract

This study investigates the impact of nitrogen doping on the performance of carbon nanotube (CNT)/polymer nanocomposites for thermoelectric applications; this was performed through measurement of conductivity of the generated nanocomposites. Three different catalysts (Co, Fe, and Ni) were used to synthesize nitrogen-doped CNTs (N-CNTs) by chemical vapor deposition technique. Synthesized N-CNTs were melt-mixed with a polyvinylidene fluoride (PVDF) matrix with a small-scale mixer at a broad range of loadings from 0.3 to 3.5 wt.% and then compression molded. Measurement of electrical conductivity of the generated nanocomposites showed superior properties in the following order of the synthesis catalyst: Co > Fe > Ni. We employed various characterization techniques to figure out the reasons behind dissimilar electrical conductivity of the generated nanocomposites, i.e., transmission electron microscopy, X-ray photoelectron spectroscopy, Raman spectroscopy, thermogravimetric analysis, light microscopy, and rheometry. It was found out, that the superior electrical conductivity of $(N\text{-}CNT)_{Co}$ nanocomposites was due to a combination of high synthesis yield, high aspect ratio, low nitrogen content, and high crystallinity of N-CNTs coupled with a good state of N-CNT dispersion. Moreover, it was revealed, that nitrogen doping had an adverse impact on electrical conductivity and, thus, on thermoelectric performance of CNT/polymer nanocomposites.

Keywords: carbon nanotube, nitrogen doping, polymer nanocomposites, electrical conductivity, thermoelectric

1. Introduction

1.1. Conductive filler/polymer nanocomposites

Conductive filler/polymer nanocomposites (CPNs) have recently drawn great interest to be employed in various applications due to their unique properties, such as tunable electrical conductivity, light weight, low cost, corrosion resistance, and processability [1, 2]. CPNs are generated by incorporating conductive filler into a polymer matrix. Conventional polymers, such as polycarbonate and polystyrene are insulative; however, incorporating conductive fillers to these polymer matrices can provide them with a broad range of conductivities through the formation of a two- or three-dimensional conductive network (**Figure 1**). Tunable electrical conductivity of CPNs entitles them to be used in a broad spectrum of applications, such as thermoelectric, charge storage, antistatic dissipation, electrostatic discharge (ESD) protection, and electromagnetic interference (EMI) shielding [3–8]. In fact, the level of electrical conductivity defines the applications in which CPNs can be employed. Charge storage and ESD protection are the major applications of CPNs necessitating low and medium electrical conductivity, respectively, whereas thermoelectric and EMI shielding require high electrical conductivity.

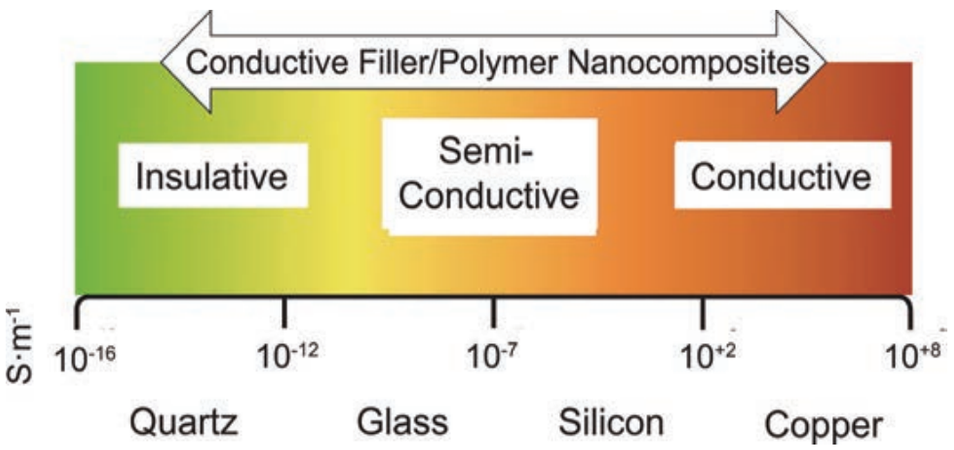

Figure 1. The approximate range of electrical conductivity covered by CPNs [1].

1.2. Conductive filler/polymer nanocomposites for thermoelectric applications

Thermoelectric devices provide an all solid-state means of heat to electricity conversion. These devices feature many advantages in heat pumps and electrical power generators, such as possessing no moving parts, generating zero noise, being easy to maintain, extended lifetime, and being highly reliable [9, 10]. However, their limited efficiency has restricted their usage to specialized applications, where cost and efficiency are of great importance. Thermoelectric efficiency is expressed in terms of dimensionless figure of merit (ZT), defined as $ZT = \frac{\alpha^2 \sigma T}{\kappa}$, in which α is Seebeck coefficient, σ is electrical conductivity, κ is thermal conductivity, and T is absolute temperature. The upper limit for thermoelectric energy conver-

http://dx.doi.org/10.5772/65675

sion efficiency is Carnot limit. Several recently developed thermoelectric materials exhibit a *ZT* near unity, resulting in efficiency equal to 10 % of the Carnot efficiency limit. By reducing the physical dimensionality of the thermoelectric materials (quantum confinement) [11], it is possible to significantly increase Seebeck coefficient and decrease the thermal conductivity. This can lead to *ZT*s as high as 3 at 550 K in n-type $PbSe_{0.98}Te_{0.02}$/PbTe quantum-dot superlattices [12]. However, application of these heavy metal thermoelectric materials is associated with high cost of material and production processes, poor processability, and huge adverse environmental impacts [13–15]. Accordingly, polymeric materials have drawn great interest to be used in thermoelectric applications. Improved processability, low cost, low thermal conductivity, and low density of polymeric materials are among key potential benefits stimulating the development of polymer-based thermoelectric materials [16, 17]. It is worth mentioning, that the figure of merit in polymer-based thermoelectric materials is $ZT \sim 0(10^{-3})$, which necessitates further investigations in this area [18].

Organic polymers exhibit poor electrical conductivity, which necessitates addition of conductive fillers in order to provide high electrical conductivity and reasonable thermoelectric performance. Recent studies suggested, that carbon-based nanofiller/polymer nanocomposites hold a significant promise in development of lightweight, low-cost thermoelectric materials [19–23]. As an instance, Yu et al. [17] demonstrated, that by forming a segregated network of carbon nanotubes (CNTs), electrical conductivities as high as 48 S cm^{-1} were achievable, while Seebeck coefficient and thermal conductivity were marginally impacted by CNT presence. This resulted in a figure of merit of 0.006 at room temperature. These findings render CNT-based polymer nanocomposite as a basis for development of thermoelectric functional materials for future green energy applications.

1.3. Nitrogen-doped carbon nanotube/polymer nanocomposites for thermoelectric applications

Different types of conductive nanofillers have been employed to develop CPNs, viz., carbonaceous nanofillers and metallic nanowires [4, 5, 24], among which, CNT has appealed remarkable attention due to its large surface area and outstanding electrical, thermal, and mechanical properties [25, 26]. The luminous era of CNTs initiated in 1991 by their discovery from soot using an arc-discharge apparatus [27]. Like fullerene and graphene, CNTs consist of a sp^2 network of carbon atoms. Among these, three carbonaceous poly-types, CNT is the only one produced in large industrial scale. There are two general types of CNTs: multi-walled CNT (MWCNT) and single-walled CNT (SWCNT). MWCNT consists of multiple rolled layers of graphite coaxially arranged around a central hollow core with van der Waals forces between contiguous layers, while SWCNT is made of a single rolled graphene [28]. The global market for CNT primary grades was $158.6 million in 2014 and is anticipated to reach $670.6 million in 2019. CNT/polymer nanocomposites represent, by far, the largest segment in the overall market of CNTs [29].

Manipulating the electronic energy gap of CNTs could lead to their superior performance. Since CNTs are sp^2 carbon systems, theoretical [30] and experimental [31] studies showed, that substituting carbon atoms with heteroatoms can result in adjustment of electronic and

structural patterns of carbon nanotubes. Nitrogen is the best choice for heteroatom substitution owing to its size proximity to carbon [32]. Bearing in mind, that nitrogen comprises one additional electron as compared to carbon, doping CNTs with nitrogen has emerged as an attractive research topic to improve the electronic properties of CNTs.

Essentially, there are three common nitrogen bonding configurations in nitrogen-doped CNTs (N-CNTs), viz., quaternary, pyridinic, and pyrrolic. As depicted in **Figure 2**, quaternary nitrogen is directly replaced for C atom in the hexagonal network, is sp^2 hybridized, and creates electron-donor state. The pyridinic nitrogen is a part of sixfold ring structure and is sp^2 hybridized, and two of its five electrons are localized sole pair. Pyrrolic nitrogen is a portion of a five-membered ring structure, is sp^3 hybridized, and gives its remaining two electrons to a π orbital, integrating the aromatic ring [33]. Whereas the quaternary and pyridinic nitrogen lead to side-wall defects, the pyrrolic nitrogen is believed to form internal cappings, generating bamboo-like sections [34]. Besides these three types, there is also possibility for N_2 molecules to get trapped inside the tube axis or intercalated into the graphitic layers of N-CNTs.

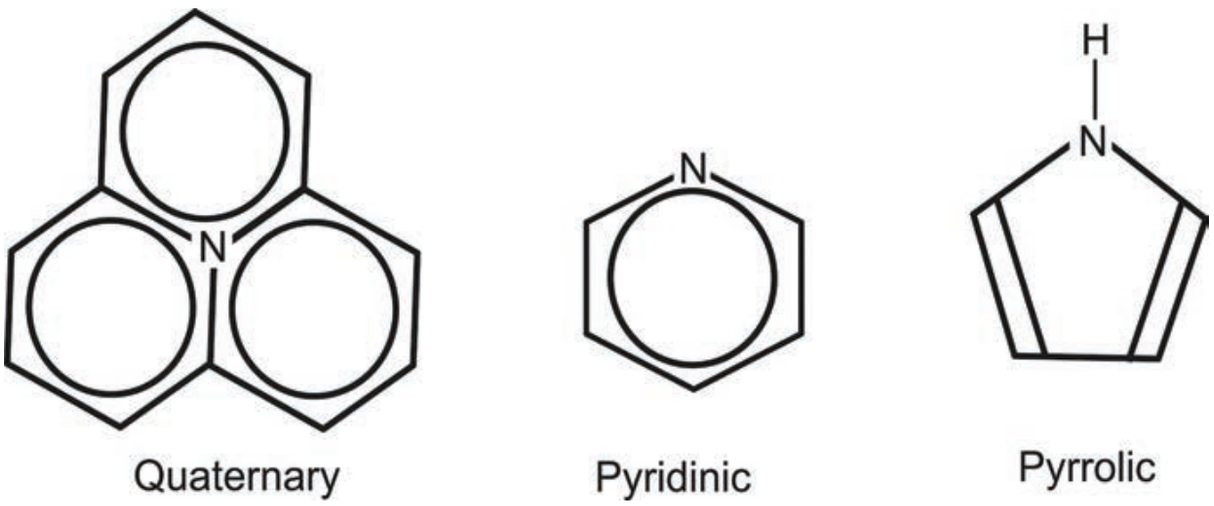

Figure 2. Major types of nitrogen bonding in N-CNTs [35].

Basically, as yet, most of the research studies have investigated the influence of nitrogen doping on electronic properties of CNTs via factors, such as density of states (DOS) and Fermi level; nevertheless, inspecting the electrical properties of polymer nanocomposites containing N-CNTs is still at its infancy [35–38]. Hence, the current study aims to research the impact of nitrogen doping on the performance of N-CNT/polymer nanocomposites for thermoelectric applications by studying its influence on electrical conductivity of N-CNT/polymer nanocomposites. N-CNTs were synthesized with different types of catalyst (Co, Fe, and Ni) to obtain diverse nitrogen contents. Afterward, synthesized N-CNTs were melt mixed into polyvinylidene fluoride (PVDF) and compression molded. We evaluated electrical conductivity of the nanocomposites at different loadings and scrutinized the underlying causes behind dissimilar conductivities of the generated nanocomposites. As high electrical conductivity of CPNs is an important factor on their performance as thermoelectric materials, this study goes significantly

http://dx.doi.org/10.5772/65675

beyond the state of the art and gives new insight on the role of nitrogen doping on conductivity and therefore performance of CNT nanocomposites for thermoelectric applications.

2. Experimental

2.1. Materials synthesis

We employed the incipient wetness impregnation technique to produce catalyst precursors. The catalyst precursors were dissolved in water and then impregnated onto aluminum oxide support (Sasol Catalox Sba-200). Thereafter, the developed materials were dried, calcinated, and reduced. Having high solubility and diffusion rate in carbon, Co, Fe, and Ni were chosen as the catalysts [39, 40]. Accordingly, we employed cobalt nitrate hexahydrate, iron (III) nitrate nonahydrate, and nickel (II) sulfate hexahydrate as the catalyst precursors. We set the metal loading at 20 wt.%. The catalyst calcination, reduction, and N-CNT synthesis were performed in CVD setup, detailed in a former study [41]. CVD setup comprised a quartz tubular reactor with an inner diameter of 4.5 cm encapsulated within a furnace. The following steps were implemented for the preparation of the catalysts: first, the catalysts were calcinated under air atmosphere with a flow rate of 100 sccm at 350 °C for 4 h. In this stage, metallic salts were translated into metal oxides. Thereafter, we used a mortar and pestle to achieve a fine powder. Hydrogen gas at a flow rate of 100 sccm at 400 °C for 1 h was utilized to obtain alumina-supported metal catalysts. Afterward, we conveyed a combination of ethane (50 sccm), ammonia (50 sccm), and argon (50 sccm) over the synthesized catalysts. Ethane played the role of carbon source, whereas ammonia and argon were nitrogen source and inert gas carrier, respectively. The synthesis temperature, synthesis time, and catalyst mass were set at 750 °C, 2 h, and 0.6 g, respectively. Catalyst preparation process is elucidated further elsewhere [39].

The polymer matrix utilized for the nanocomposite preparation was semicrystalline PVDF 11008/0001, purchased from 3M Canada, with an average density of 1.78 g/cm^3 and melting point of 160 °C. PVDF was opted as the polymer matrix owing to its ferroelectricity, high dielectric strength (~13 kV mm^{-1}), corrosion resistance, good mechanical properties, thermal stability, good chemical resistance (excellent with acid and alkali), and robust interaction of electrophilic fluorine groups with CNTs [42–44]. The mixing of synthesized N-CNTs with PVDF matrix was carried out with Alberta Polymer Asymmetric Minimixer (APAM) at 240 °C and 235 rpm. PVDF matrix was first masticated within the mixing cup for 3 min, and then N-CNTs were inserted and mixed for an additional 14 min. For each catalyst, the nanocomposites with different N-CNT concentrations, i.e., 0.3, 0.5, 1.0, 2.0, 2.7, and 3.5 wt.%, were prepared. The nanocomposites were molded into circular cavities with 0.5 mm thickness using Carver compression molder (Carver Inc.) at 220 °C under 38 MPa pressure for 10 min. The molded samples were used for electrical, morphological, and rheological characterizations.

2.2. Materials characterization

2.2.1. N-CNT characterization

2.2.1.1. Transmission electron microscopy of N-CNTs

High-resolution transmission electron microscopy (HRTEM) was used to inspect the morphology of synthesized N-CNTs. HRTEM was conducted on Tecnai TF20 G2 FEG-TEM (FEI) at 200 kV acceleration voltage with a standard single-tilt holder. The images were taken with Gatan UltraScan 4000 CCD camera at 2048 × 2048 pixels. For HRTEM, around 1.0 mg of N-CNT powder was dispersed in 10 mL ethanol and bath sonicated for 15 min. A drop of the dispersion was mounted on the carbon side of a standard TEM grid covered with a ~40 nm holey carbon film (EMS). Measurement of the geometrical dimensions of N-CNTs was conducted for over 100 individual ones utilizing MeasureIT software (Olympus Soft Imaging Solutions GmbH).

2.2.1.2. X-ray photoelectron spectroscopy, Raman spectroscopy and thermogravimetric analysis

PHI VersaProbe 5000-XPS was used to obtain X-ray photoelectron spectra. The spectra were achieved employing monochromatic Al source at 1486.6 eV and 49.3 W with a beam diameter of 200.0 μm. The structural defects of N-CNTs were inspected using Raman spectroscopy. Renishaw inVia Raman microscope was used to obtain Raman spectra. Excitation was provided by the radiation of an argon-ion laser beam with 514 nm wavelength. A 5× objective was used to get Raman spectra. The yield of the synthesis process was inspected with Thermogravimetric Analyzer (TA instruments, Model: Q500). The samples were heated under air atmosphere (Praxair AI INDK) from ambient temperature to 950 °C at a rate of 10 °C/min. The samples were kept at 950 °C for 10 min before cooling.

2.2.2. Nanocomposite characterization

2.2.2.1. Light microscopy

The microdispersion state of the nanofillers within PVDF matrix was enumerated using light transmission microscopy (LM) on thin cuts (5 μm thickness) of the compression-molded samples, prepared with Leica Microtome RM 2265 (Leica Microsystems GmbH). Olympus BH2 optical microscope (Olympus Deutschland GmbH) equipped with CCD camera DP71 was used to capture images with dimensions of 600 μm × 800 μm from different cut sections. The software Stream Motion (Olympus) was used to analyze the images. The agglomerate area ratio (in %) was defined by dividing the spotted area of non-dispersed nanofillers (with equivalent circle diameter > 5 μm, area > 19.6 μm^2) over the whole sample area (15 cuts, ca. 7.2 mm^2). Mean value and standard deviation, demonstrating the differences between the cuts and thus heterogeneity, were reckoned. The relative transparency of the cuts provided added information about the amount of dispersed nanofillers in the samples. The relative transparency was quantified by dividing the transparency of the cut over the transparency of the glass slide/cover glass assembly. Ten various areas per sample were used to obtain mean values and

http://dx.doi.org/10.5772/65675

standard deviations. Further information on employing LM to evaluate microdispersion state of nanofillers within nanocomposites is presented elsewhere [45, 46].

2.2.2.2. TEM

Ultrathin sections of the samples were cut using ultramicrotome EM UC6/FC6 (Leica) setup with an ultrasonic diamond knife at ambient temperature. The sections were floated off water and thereafter transferred on carbon-filmed TEM copper grids. TEM characterizations were carried out employing TEM LIBRA 120 (Carl Zeiss SMT) with an acceleration voltage of 120 kV.

2.2.2.3. Rheology

Rheological measurements were performed using Anton-Paar MCR 302 rheometer at 240 °C using 25 mm cone-plate geometry with a cone angle of 1° and truncation of 47 μm. The thermal stability of the prepared samples was validated by conducting small-amplitude oscillatory shear measurements prior to and following the long-time exposure of the samples to elevated temperatures. Various rheological properties were measured at 240 °C to characterize the linear and nonlinear response for the neat and nanocomposite samples.

2.2.2.4. Electrical conductivity

Two conductivity meters with 90 V as the applied voltage were employed to measure the electrical conductivity of the generated materials. For nanocomposites with an electrical conductivity higher than 10^{-2} S m^{-1}, the measurements were conducted according to ASTM 257-75 standards employing Loresta GP resistivity meter (MCP-T610 model, Mitsubishi Chemical Co.). An ESP probe was used to avert the effect of contact resistance. For electrical conductivities less than 10^{-2} S m^{-1}, the measurements were carried out with Keithley 6517A electrometer connected to Keithley 8009 test fixture (Keithley Instruments).

3. Results and discussion

3.1. General background

3.1.1. Mechanisms of electrical conductivity

Electrical conductivity derives from ordered movement of charge carriers (electric current). In the absence of an electric field, the conduction electrons are scattered freely in a solid owing to their thermal energy. If an electric field, E, is applied, the force on an electron, e, is $-eE$, and the electron is accelerated in the opposite direction to the electric field because of its negative charge. Accordingly, there is a net velocity and the current density is presented by [47]:

$$J = N_e \times e \times \mu \times E, \tag{1}$$

where J is the current density, N_e is concentration of electrons, e is charge of electron, μ is the electron mobility, and E is the applied electric field. The applied electric field equals to the applied voltage over the thickness of a sample. Hence, the electrical conductivity can be determined as:

$$\sigma = \frac{J}{E}, \tag{2}$$

where σ is electrical conductivity and its SI unit is Siemens per meter (S m^{-1}). Electrical conductivity of materials is an intrinsic property, which spans a very wide range. The conductivity of insulators is typically less than 10^{-10} S m^{-1}, that of semiconductive materials covers the range 10^{-10} to around 10^{-2} S m^{-1}, and for semimetals and metals is more than 10^{-2} S m^{-1}.

Electrical conductivity of materials can be elucidated employing the band theory [48]. In the band theory, the energy level of each electron is reflected as a horizontal line. As any solid possesses a large number of electrons with various energy levels, the sets of energy levels form two continuous energy bands, named valence band and conduction band. The energy gap between the two bands signifies the forbidden region for electrons. Electrons restrained to individual atoms or interatomic bonds are, in the band theory, said to be in valence band. Those electrons, that can move freely in substance upon applying electric field lie in conduction band. **Figure 3** depicts a schematic of the bands in a solid identifying three main types of materials: insulators, semiconductors, and metals. Valence and conduction bands in metals overlap each other; therefore, metals indicate very high conductivity. In intrinsic semiconductors, the valence-conduction band gap is adequately small, so that, electrons in valence band can be excited to conduction band by thermal energy. Among the three types of materials illustrated in **Figure 3**, insulators show the largest valence-conduction band gap, and, therefore, fewer electrons can be excited to their conduction band by thermal energy. This results in a very low conductivity in insulators.

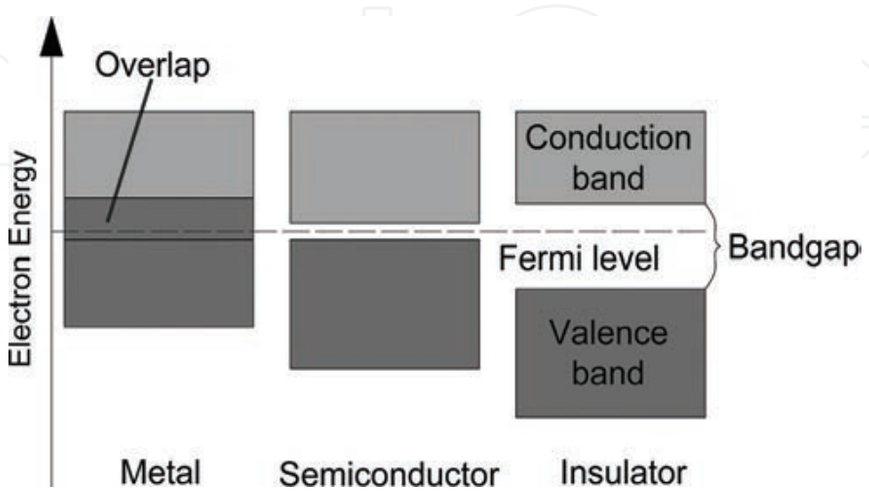

Figure 3. Simplified diagram of the electronic band structure in the band theory, reproduced from [34].

http://dx.doi.org/10.5772/65675

3.1.2. Electrical conductivity in CPNs

High electrical conductivity, i.e., conductive network formation, at very low filler contents has made CPNs distinctive materials for industrial applications [25, 26]. Conductive network formation in CPNs is better understood with the concept of percolation threshold [49, 50]. Percolation means, that at least one conductive pathway forms to allow electrical current to pass across CPNs, thereby transforming CPNs from insulative to conductive. Percolation happens at a narrow filler concentration range, where the electrical conductivity of CPNs drastically increases by several orders of magnitude. Low electrical percolation threshold in CPNs leads to the production of cost-effective composites.

Many statistical, geometric, thermodynamic, and structure-based models have been introduced to anticipate the percolation threshold and electrical conductivity of CPNs [49, 51]. Although the percolation theory is just valid at conductive filler concentrations above the percolation threshold, it is the most acceptable one. Statistical percolation theory estimates the percolation threshold of CPNs as:

$$\sigma = \sigma_0 \cdot \left(V - V_c\right)^t, \tag{3}$$

where σ is electrical conductivity of CPN, σ_0 is electrical conductivity of conductive filler, V is dimensionless volume content of conductive filler, and V_c and t are percolation threshold and critical exponent, respectively [49]. The equation is valid for filler concentration above the percolation threshold, i.e., $V > V_c$. Higher t value and lower percolation threshold correspond to well-dispersed, high-aspect-ratio fillers [52–54].

Figure 4 illustrates a typical percolation curve of CPNs [55]. In general, percolation curve of CPNs can be divided into three regions: (1) region far below the percolation threshold (insulative region), (2) region where percolation occurs (percolation region), and (3) region far above the percolation threshold (conductive region). In the insulative region, the conductive filler loading is very low with the fillers far from each other; thus, polymer matrix dominates the charge transfer. As a matter of fact, at low filler concentrations, the insulating gaps are very large and the chance, that nomadic charge carriers are transferred between conductive fillers is very low.

By enhancing filler loading, the gaps between conductive fillers decrease, and a drastic increase in electrical conductivity is observed over a narrow concentration range (percolation region). In this region, hopping and direct-contact mechanisms become significant. When the mean particle-particle distance reaches below 1.8 nm, the dominant electron transfer mechanism become hopping mechanism [56–58]. It is reported, that the presence of large conductive agglomerates in CPN results in a very high secondary internal electric field between the conductive islands [57, 59]. This high field strength assists free electrons in conductive filler having adequate energy to hop over the insulative gaps. Nevertheless, hopping takes place when an electron receives sufficient energy to pass over distance to nearest free site with lower energy to alter its lattice site. In the percolation region, due to proximity or direct contact of conductive fillers, the nomadic charge carriers in conductive fillers play the dominant role in

conduction mechanism. Since these free charge carriers belong to the conduction band, the conductivity of the nanocomposite rises by several orders of magnitude in the percolation region. Next, by adding more filler loading, a well-developed, 3D conductive network initiates to form, but the electrical conductivity increases only marginally. This is due to substantial current dissipation at the contact spots between conductive fillers, i.e., the constriction resistance, leading to a plateau in the percolation curve [26].

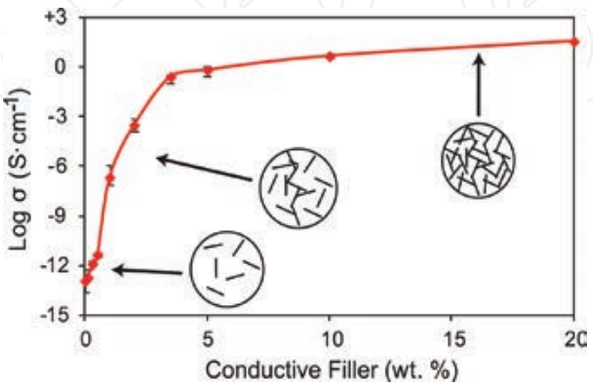

Figure 4. Percolation curve of compression-molded CNT/polystyrene nanocomposite (a typical percolation curve of CPNs) [55].

3.2. Electrical conductivity of N-CNT/PVDF nanocomposites

The percolation curves of N-CNT/PVDF nanocomposites are depicted in **Figure 5**. It was observed, that $(N\text{-}CNT)_{Co}$/PVDF nanocomposites presented the lowest percolation threshold (1.5 wt.%) and highest electrical conductivity (3 S m^{-1} at 3.5 wt.%). However, it was revealed, that Ni-based nanocomposites were insulative up to 2.7 wt.% and experienced a slight increase in electrical conductivity at 3.5 wt.%. The Fe-based nanocomposites presented an increase in electrical conductivity from 1.0 wt.% to 3.5 wt.% with a mild slope.

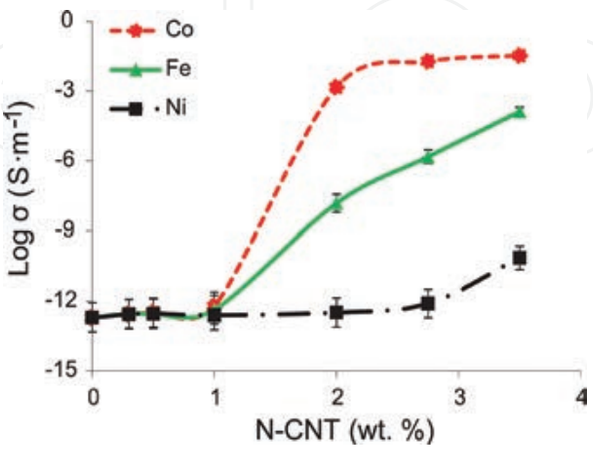

Figure 5. Electrical conductivity of N-CNT/PVDF nanocomposites as a function of N-CNT content. N-CNTs were synthesized over Co, Fe, and Ni catalysts.

http://dx.doi.org/10.5772/65675

There are many factors impacting the electrical conductivity of CPNs, such as loading, intrinsic conductivity, size, and aspect ratio of conductive filler, inherent properties of polymer medium, interfacial properties of CPN constituents, dispersion and distribution of filler, blending method, and crystalline structure of the matrix. The impacts of the aforementioned parameters on electrical conductivity of CNT/polymer nanocomposites have been well reviewed in the literature [1, 60–62]. Accordingly, in succeeding section, we scrutinize structural and morphological features of N-CNTs and their nanocomposites to figure out the reasons behind different electrical behaviors of the generated nanocomposites.

3.3. Morphological and structural characterization of N-CNTs

The morphology and graphitic structure of N-CNTs were analyzed using TEM images. **Figure 6** indicates, that the type of synthesis catalyst played a leading role in creating the final morphology of N-CNTs. As depicted in **Figure 6**, we observed an open-channel morphology for $(N\text{-}CNT)_{Co}$ and a bamboo-like morphology for $(N\text{-}CNT)_{Fe}$ and $(N\text{-}CNT)_{Ni}$. Surface roughness is observed in bamboo-like N-CNTs, deriving from defected bonding of bamboo-like sections. The flawed parts in the wall of N-CNTs are attributed to replacement of nitrogen atoms [63, 64]. Since an open-channel structure was formed for $(N\text{-}CNT)_{Co}$, we can say, that other factors, than nitrogen bonding, are involved in creation of bamboo-like morphology, such as type of catalyst.

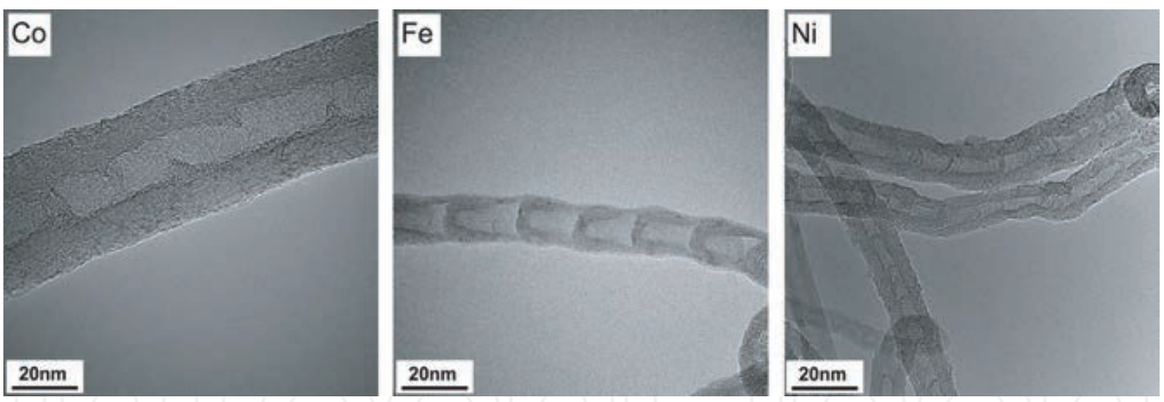

Figure 6. TEM micrographs of N-CNTs synthesized over Co, Fe, and Ni catalysts.

Table 1 tabulates average length and diameter, nitrogen content, Raman feature, and synthesis yield of synthesized N-CNTs. We perceived, that N-CNTs synthesized over Fe catalyst had the largest diameter, over double that of $(N\text{-}CNT)_{Ni}$. Statistical analysis of particle size of the catalysts revealed a good correlation between diameter of N-CNTs and size of catalyst particles. Discrepancies in original size of the catalyst particles and also dissimilar tendencies of the catalyst particles to sinter at synthesis temperatures are among significant parameters affecting the variation in diameter of N-CNTs. It should be noted, that metallic nanoparticles with sizes below 10 nm experience a drastic drop in melting point [65]. High synthesis temperature range (600–1000 °C) coupled with exothermic thermal decomposition of the precursor molecules

results in higher temperature than nominal reaction temperature, contributing to metal liquefaction and coalescence of catalyst particles [66, 67].

	Co	Fe	Ni
Length (μm)	2.6	2.6	1.2
Diameter (nm)	25	46	20
Nitrogen content (at.%)	2.2	2.2	3.3
I_D/I_G	0.79	0.73	0.81
Synthesis yield %	89.5	85.1	63.9

Table 1. Physical and structural features of N-CNTs synthesized over Co, Fe, and Ni catalysts.

Table 1 shows, that $(N\text{-}CNT)_{Co}$ and $(N\text{-}CNT)_{Fe}$ had average length about 2.6 μm, while $(N\text{-}CNT)_{Ni}$ exhibited considerably lower average length about 1.2 μm. The shorter length of $(N\text{-}CNT)_{Ni}$ can be attributed to either inferior activity of Ni catalyst, as will be shown by TGA, or the presence of larger amount of nitrogen in their structure, as will be exhibited by X-ray photoelectron spectroscopy (XPS) analysis. The presence of nitrogen can be envisaged as an important factor to bend, close, and cap N-CNTs. It is worth noting, that average length and diameter of N-CNTs are of high significance for electrical applications, since CNTs with high aspect ratio provide CPNs with superior electrical performance [68, 69].

The amount of nitrogen content can have a weighty effect on morphological, physical, and electronic properties of N-CNTs. The achieved data revealed, that atomic content of nitrogen incorporated into $(N\text{-}CNT)_{Ni}$ was 3.3 at.%, whereas $(N\text{-}CNT)_{Co}$ and $(N\text{-}CNT)_{Fe}$ had considerably lower nitrogen content, i.e., 2.2 at.%. As nitrogen could have the effect of closing the tube structures and thereby developing more disordered, bent, and capped structures, the larger nitrogen content of $N\text{-}CNT_{Ni}$ could be a contributing factor to its lower length.

In Raman spectra of CNTs, tangential mode (*G* band) and defect-active mode (*D* band) offer valuable information about physical and electronic structure of CNTs [70, 71]. Hence, Raman spectroscopy was used to inspect the influence of nitrogen doping on physical and morphological features of N-CNTs. *G* band (~1600 cm^{-1}) derives from the stretching of C─C bond in graphitic materials and is mutual to all sp^2 carbon forms. *D* band (~1400 cm^{-1}) is double-Raman scattering process, which requires lattice distortion to break the basic symmetry of the graphitic structure [72]. Therefore, the presence of structural defects stimulates *D* band feature. Accordingly, the ratio of *D* and *G* band intensities is often used as indicative tool to validate the structural perfection of CNTs [73]. We observed, that $(N\text{-}CNT)_{Ni}$ had the uppermost I_D/I_G ratio, signifying the poorest crystallinity. These results are in line with TEM images of $(N\text{-}CNT)_{Ni}$, indicating poorer crystalline morphology than the other forms of N-CNTs. Moreover, Villalpando-Paez et al. [74] and Ibrahim et al. [75] reported good correlation between nitrogen concentration and I_D/I_G ratio. This is in agreement with our study and shows the opposing influence of nitrogen doping on the crystalline structure of N-CNTs. We also observed, that

http://dx.doi.org/10.5772/65675

$(N\text{-}CNT)_{Ni}$ went through more breakage during the melt mixing process, ascribed to its poorer crystallinity.

TGA analysis helped investigate the synthesis yield. We obtained residues of 11.5 %, 14.9 %, and 36.1 %, relative to original mass, for $(N\text{-}CNT)_{Co}$, $(N\text{-}CNT)_{Fe}$, and $(N\text{-}CNT)_{Ni}$, respectively. The residue consists of metallic oxide particles and alumina substrate [41, 76]. The higher the yield of the synthesis process, the lower is the amount of the remaining residue. Thus, we can claim, that Ni catalyst had an inferior performance compared to Co and Fe catalysts. The catalyst particles contained 80 wt.% alumina and 20 wt.% metallic particles. Alumina is insulative and metallic particles have much less surface area than synthesized N-CNTs, and their surface area even further reduced due to sintering phenomenon. This justifies the significance of synthesis yield on electrical properties.

3.4. Morphological characterization of N-CNT/PVDF nanocomposites

The dispersion state of conductive filler within polymer matrix is intensely influential on electrical properties. Hence, we inspected the dispersion state at three various scales. Micro-dispersion state of N-CNTs within the polymer medium was investigated via LM. LM talks about the portion of fillers, that appears as big agglomerates and is not disentangled well, and was enumerated as the agglomerate area ratio in our study. Moreover, gray appearance of LM samples helps us quantify the agglomerates with sizes equal to or slightly larger than the wavelength of visible light, ca. 400–700 nm, but smaller than visually identifiable agglomerates. Darker background denotes more nanotubes dispersed in this range. We also employed TEM to obtain information about nanodispersion state of carbon nanotubes, i.e., how well carbon nanotubes disentangle individually.

Figure 7 portrays examples for LM images of three different nanocomposites, corresponding to different synthesis catalysts, with 2.0 wt.% N-CNT content. Quantification of the agglomerate area ratio, as shown in **Table 2**, illustrates the lowest agglomerate area ratio for samples containing Fe-based N-CNTs, followed by Co and Ni. The corresponding relative transparency values indicate the lowest value for Co-based N-CNTs, followed by Fe-based and Ni-based.

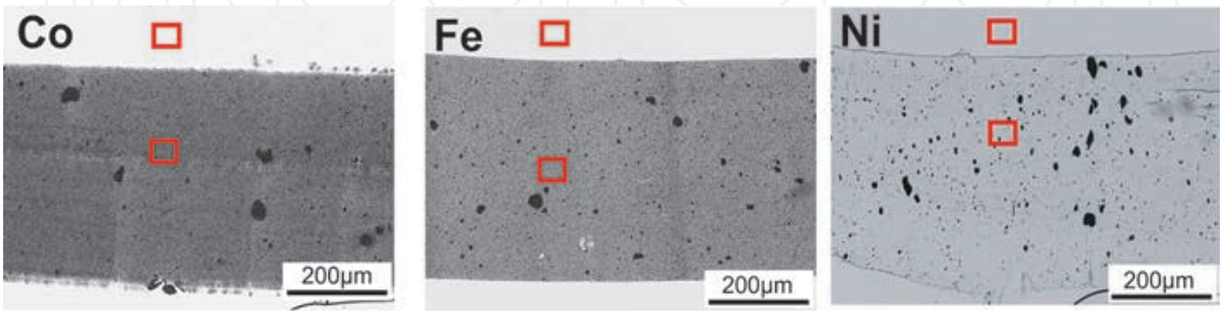

Figure 7. LM images of microtomed sections of 2.0 wt.% N-CNT/PVDF nanocomposites. N-CNTs were synthesized over Co, Fe, and Ni catalysts. The red squares represent areas employed for relative transparency quantifications.

	Co	Fe	Ni
Agglomerate area ratio %	2.3	1.8	2.8
Relative transparency %	37	53	86

Table 2. LM microdispersion parameters of microtomed N-CNT/PVDF nanocomposites with N-CNTs synthesized over different catalysts.

TEM images look into nanodispersion state of N-CNTs in PVDF medium (**Figure 8**). The images clearly show, that $(N\text{-}CNT)_{Ni}$ had the worst dispersion state. TEM image of $(N\text{-}CNT)_{Ni}$/PVDF nanocomposite shows a few individual nanotubes beside fairly large agglomerates. $(N\text{-}CNT)_{Co}$ presented the best state of nanodispersion, while $(N\text{-}CNT)_{Fe}$/PVDF nanocomposites held small agglomerates with sizes around 500 nm. In conclusion, microscopy images showed, that $(N\text{-}CNT)_{Co}$ and $(N\text{-}CNT)_{Fe}$ had better both microdispersion and nanodispersion than their Ni-based counterpart. Co-based and Fe-based N-CNTs indicated only marginal discrepancies in their dispersion state.

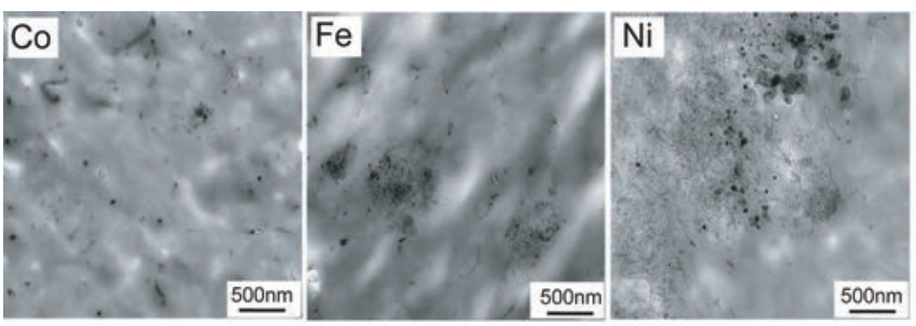

Figure 8. TEM images of 2.0 wt.% N-CNT/PVDF nanocomposites with N-CNTs synthesized with different catalysts, illustrating nanodispersion state of N-CNTs.

3.5. Linear and nonlinear melt-state rheological response of N-CNT/PVDF nanocomposites

Figure 9 depicts storage modulus (G') and loss modulus (G'') of N-CNT/PVDF nanocomposites as a function of frequency under small-amplitude oscillatory shear (γ = 1 %) for a frequency range from 0.1 rad/s to 625 rad/s at 240 °C.

As shown in **Figure 9**, G' in low frequency region (ω ~ 0.1 rad/s) is significantly larger than G'' (a damping factor smaller than unity) for $(N\text{-}CNT)_{Co}$/PVDF and $(N\text{-}CNT)_{Ni}$/PVDF nanocomposites at concentrations as low as 0.5 wt.%. $(N\text{-}CNT)_{Fe}$/PVDF nanocomposite samples, however, exhibited an elastic dominant response ($G' > G''$) only at very high nanofiller concentrations (~2.0 wt.%). It is noticeable, that all N-CNT/PVDF nanocomposites, regardless of synthesis catalyst, showed a signature for the existence of an ultraslow relaxation process (a near-zero slope for G' in low frequency region) at concentrations as low as 0.5 wt.%. This indicates, that linear rheological response was affected by the presence of N-CNTs at concentrations, that no significant enhancement in electrical conductivity was observable in N-CNT nanocomposites.

http://dx.doi.org/10.5772/65675

The linear melt-state rheological response is mainly controlled by several factors, such as inter-tube van der Waals interactions, micro- and nanodispersion states, individual CNT stiffness, and CNT network stiffness [77–79]. Individual CNT stiffness is mainly controlled by intra-wall C—C bond strength and graphitic interlayer load transfer [80]. This suggests, that structural imperfections and defects in CNT graphitic walls can deteriorate their elastic properties. Moreover, stiffness of the network structure formed by CNT bundles is mainly determined by the load transfer across CNT/polymer and CNT-CNT interface [79]. In this context, it could be mentioned, that a scenario entirely based on individual CNT stiffness may not be able to fully describe the observations for elastic response of N-CNT nanocomposites in low frequency region. As can be seen in **Figure 9**, Co-, Fe-, and Ni-based N-CNT nanocomposites reached a storage modulus of 9640 Pa, 2290 Pa, and 3860 Pa at 0.1 rad, respectively. The presence of higher amount of structural imperfections may not be responsible for lower elasticity observed for Fe-based N-CNT nanocomposite as $(N\text{-}CNT)_{Fe}$ showed the lowest I_D/I_G. Therefore, the main contributing factors to linear melt-state rheological observations could be considered as the dispersion state and load transfer across the interfacial region.

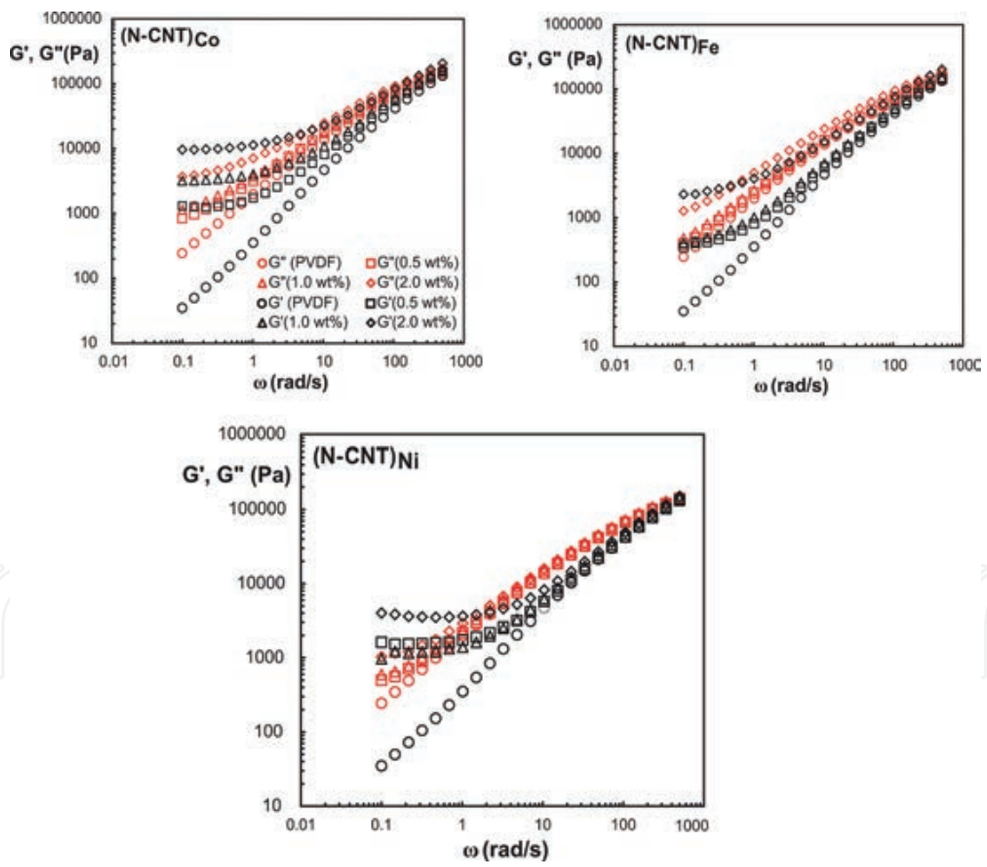

Figure 9. Small amplitude oscillatory shear response at γ = 1 % and T = 240 °C for neat PVDF and N-CNT/PVDF nanocomposites with N-CNTs synthesized over different catalysts.

Figure 10 depicts oscillatory amplitude sweep response of neat PVDF and N-CNT/PVDF nanocomposites containing 3.5 wt.% N-CNTs synthesized over different catalysts over a

range of applied strain amplitudes from 0.1 to 1000.0 % at an angular frequency of 0.1 rad/s. The responses observed for neat PVDF and N-CNT/PVDF nanocomposite samples demonstrated a transition from a linear regime to a nonlinear regime and also a drop in G' as strain amplitude increases. It is noticeable, that in low-strain region, all nanocomposite samples exhibited elastic dominant response ($G' > G''$). These results also feature a crossover strain amplitude γ_x ($G' = G''$), which is a measure of N-CNT network sensitivity to deformation-induced microstructural changes. As shown in **Figure 10**, Co-, Fe-, and Ni-based N-CNT nanocomposites exhibited crossover strain amplitudes of 32.0 %, 5.8 %, and 5.6 %, respectively. This implies, that Co-based N-CNTs featured a very resilient behavior toward the applied deformation field and the stress-bearing backbone of the fractal clusters survived up to strain amplitudes one order of magnitude larger than N-CNTs synthesized over Fe and Ni. It is noticeable, that Ni-based N-CNT nanocomposite showed a multistep transition into a nonlinear regime as G' dropped to an intermediate plateau and then significantly decreased. Moreover, the first step decrease in G' in $(\text{N-CNT})_{\text{Ni}}$ nanocomposite was accompanied by a dissipation process signified by a weak local peak in G''.

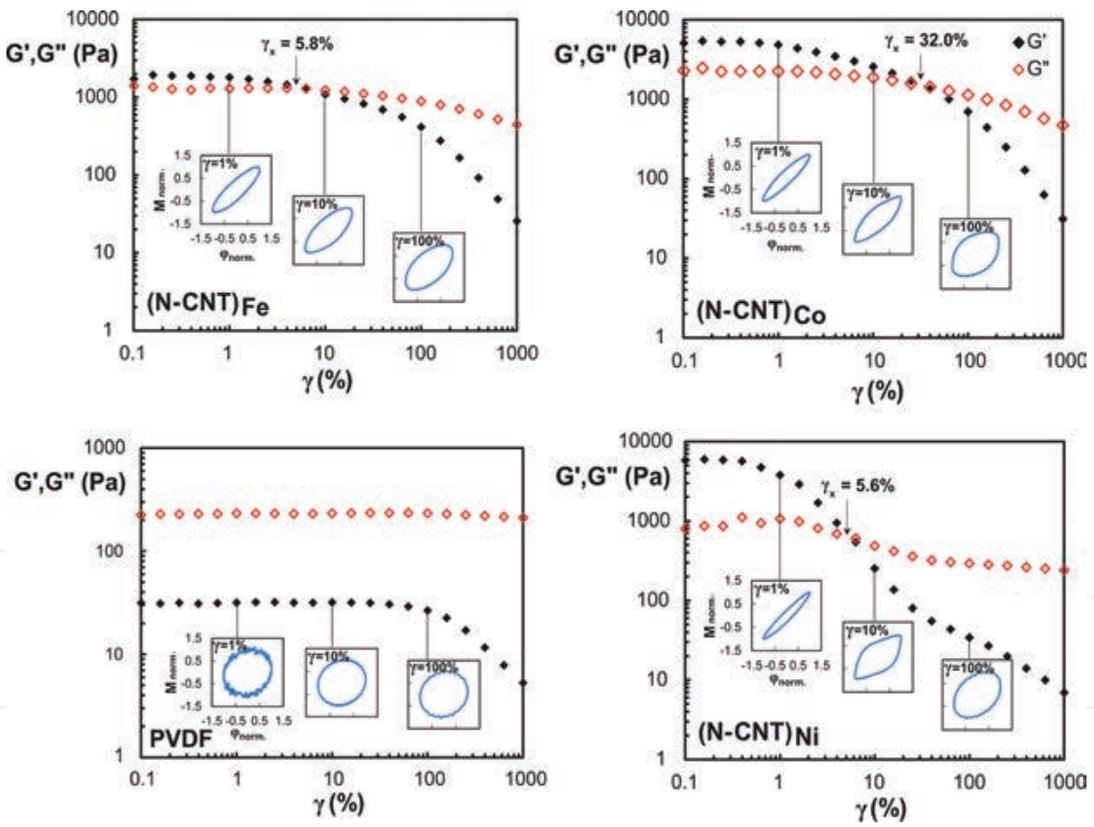

Figure 10. Oscillatory amplitude sweep response of neat PVDF and N-CNT/PVDF nanocomposites containing 3.5 wt.% N-CNTs synthesized over different catalysts for strain amplitudes of γ_0 = 0.1–1000 % at an angular frequency of ω = 0.1 rad/s. The insets show the non-dimensionalized elastic Lissajous loops for strain amplitudes indicated by solid lines.

Insets in **Figure 10** depict non-dimensionalized elastic Lissajous loops [81–83], in which normalized torque $M_{norm.}$ is plotted as a function of normalized deflection angle $\phi_{norm.}$. At small strain amplitudes (γ ~ 1.0 %), for neat PVDF and nanocomposites, elastic Lissajous loops were

http://dx.doi.org/10.5772/65675

elliptical, corresponding to a linear viscoelastic response. The area enclosed by elastic Lissajous loops is significantly smaller in N-CNT nanocomposites than neat PVDF, indicating an elastic dominant response in this region. As strain amplitude increased, Lissajous loops in N-CNT nanocomposite samples became distorted, indicative of thixotropy and a yielding process in nanocomposite samples. Furthermore, observed patterns for nanocomposites suggest that N-CNT at-rest microstructure partially survived in both weakly ($\gamma \sim \gamma_x$) and strongly ($\gamma > \gamma_x$) nonlinear regimes as the area enclosed by Lissajous loops is relatively smaller, than that observed for neat PVDF. The area enclosed by elastic Lissajous loops in weakly and strongly nonlinear regimes for N-CNT nanocomposites showed the following order: Ni > Fe ~ Co.

As demonstrated by LM observations, Ni-based N-CNT nanocomposite presented the highest agglomerate area and relative transparency, indicating a poor dispersion quality of N-CNTs within PVDF matrix. This could be responsible for observing a multistep transition into a nonlinear regime and strongly nonlinear response at intermediate strain amplitudes in Ni-based N-CNT samples. As explained in the preceding section, N-CNTs synthesized over different catalysts demonstrated fundamentally different dispersion states at different scales. The presence of densely aggregated N-CNT structures in Ni-based N-CNT nanocomposite led to poor load transfer across polymer-aggregate interface, resulting in deformation-induced microstructural changes initiated from aggregate-aggregate boundaries at intermediate strain amplitudes ($\gamma \sim \gamma_x$). This was followed by widespread disintegration of $(\text{N-CNT})_{\text{Ni}}$ aggregates, marked by multistep transition into a nonlinear regime. However, in Co-based and Fe-based N-CNT nanocomposites, the transition into nonlinear regime occurred by *stochastic erosion* [84, 85] of network structures formed by individually dispersed N-CNTs bound polymer chains and polymer matrix entanglement network [86, 87].

In this context, it could be added, that Fe-based N-CNT nanocomposites demonstrated a dual nature in a sense, that it showed an almost one-step transition into a nonlinear regime; however, the crossover point occurred at fairly small strain amplitude (γ_x = 5.8 %). This dual behavior can be explained in conjunction with poorer load transfer across interfacial region than Co-based N-CNT nanocomposite as a result of denser N-CNT clusters present in Fe-based N-CNT nanocomposite. Moreover, one-step transition to a nonlinear regime compared to the multistep transition observed for Ni-based N-CNT nanocomposite can be attributed to better nanodispersion state achieved in Fe-based N-CNT nanocomposite (see TEM images in **Figure 8** and relative transparency values in **Table 2**). Overall, it can be expressed, that no direct link between individual N-CNT structural features and rheological response was detectable, and thus N-CNT dispersion state played the main role in determining the melt-state rheological response.

4. Conclusions

In brief, this study revealed, that electrical conductivity of N-CNT/PVDF nanocomposites is highly dependent on N-CNT synthesis catalyst. Measuring electrical conductivity of the generated nanocomposites showed superior electrical conductivity and, thus, thermoelectric performance in the following order of the synthesis catalyst: Co > Fe > Ni. It was observed, that

a combination of high synthesis yield, high aspect ratio, low structural defects, enhanced network formation, and good state of N-CNT dispersion can provide N-CNT/PVDF nanocomposites with superior electrical conductivity. Moreover, it was revealed, that nitrogen doping had an adverse impact on electrical conductivity of CNT/polymer nanocomposites and, therefore, their performance as thermoelectric materials.

Acknowledgements

Financial support from the Natural Sciences and Engineering Research Council of Canada (NSERC) is highly appreciated. We would like to thank Prof. Uttandaraman Sundararaj for his supervision to perform this project. We are grateful to Dr. Lars Laurentius for his assistance with Raman spectroscopy. In addition, we thank Dr. Petra Pötschke and Ms. Uta Reuter from IPF Dresden for LM and TEM investigations. Dr. Mohammad Arjmand thanks IPF Dresden for granting a research stay.

Author details

Mohammad Arjmand* and Soheil Sadeghi

*Address all correspondence to: arjmand64@yahoo.com

University of Calgary, Calgary, Canada

References

[1] Arjmand M. Electrical Conductivity, Electromagnetic Interference Shielding and Dielectric Properties of Multi-walled Carbon Nanotube/Polymer Composites [thesis]. Calgary: University of Calgary; 2014.

[2] Al-Saleh MH. Nanostructured Conductive Polymeric Materials [thesis]. Edmonton: University of Alberta; 2009.

[3] McGrail BT, Sehirlioglu A, Pentzer E. Polymer composites for thermoelectric applications. Angewandte Chemie-International Edition. 2015;54:1710–23. DOI: 10.1002/anie.201408431.

[4] Arjmand M, Moud AA, Li Y, Sundararaj U. Outstanding electromagnetic interference shielding of silver nanowires: comparison with carbon nanotubes. RSC Advances. 2015;5:56590–8. DOI: 10.1039/C5RA08118A.

[5] da Silva AB, Arjmand M, Sundararaj U, Bretas RES. Novel composites of Copper nanowire/PVDF with superior dielectric properties. Polymer. 2014;55:226–34. DOI: 10.1016/j.polymer.2013.11.045.

[6] Pawar SP, Arjmand M, Gandi M, Bose S, Sundararaj U. Critical insights into understanding the effects of synthesis temperature and nitrogen doping towards charge storage capability and microwave shielding in nitrogen-doped carbon nanotube/polymer nanocomposites. RSC Advances. 2016;6:63224–34. DOI: 10.1039/C6RA15037C.

[7] Arjmand M, Mahmoodi M, Park S, Sundararaj U. Impact of foaming on the broadband dielectric properties of multi-walled carbon nanotube/polystyrene composites. Journal of Cellular Plastics. 2014;50:551–62. DOI: 10.1177/0021955X14539778.

[8] Arjmand M, Sundararaj U. Broadband dielectric properties of multiwalled carbon nanotube/polystyrene composites. Polymer Engineering & Science. 2015;55:173–9. DOI: 10.1002/pen.23881.

[9] Liu W, Yan X, Chen G, Ren Z. Recent advances in thermoelectric nanocomposites. Nano Energy. 2012;1:42–56. DOI: 10.1016/j.nanoen.2011.10.001.

[10] Bell LE. Cooling, heating, generating power, and recovering waste heat with thermoelectric systems. Science. 2008;321:1457–61. DOI: 10.1126/science.1158899.

[11] Dresselhaus MS, Chen G, Tang MY, Yang RG, Lee H, Wang DZ, et al. New directions for low-dimensional thermoelectric materials. Advanced Materials. 2007;19:1043–53. DOI: 10.1002/adma.200600527.

[12] Li G, Gadelrab KR, Souier T, Potapov PL, Chen G, Chiesa M. Mechanical properties of $Bi_xSb_{2-x}Te_3$ nanostructured thermoelectric material. Nanotechnology. 2012;23:065703. DOI: 10.1088/0957-4484/23/6/065703.

[13] Li J, Tang X, Li H, Yan Y, Zhang Q. Synthesis and thermoelectric properties of hydrochloric acid-doped polyaniline. Synthetic Metals. 2010;160:1153–8. DOI: 10.1016/j.synthmet.2010.03.001.

[14] Toshima N. Conductive polymers as a new type of thermoelectric material. Macromolecular Symposia. 2002;186:81–6. DOI: 10.1002/1521-3900(200208)186:1<81::AID-MASY81>3.0.CO;2-S.

[15] Yao Q, Chen L, Zhang W, Liufu S, Chen X. Enhanced thermoelectric performance of single-walled carbon nanotubes/polyaniline hybrid nanocomposites. ACS Nano. 2010;4:2445–51. DOI: 10.1021/nn1002562.

[16] Yu B, Zebarjadi M, Wang H, Lukas K, Wang H, Wang D, et al. Enhancement of thermoelectric properties by modulation-doping in silicon germanium alloy nanocomposites. Nano Letters. 2012;12:2077–82. DOI: 10.1021/nl3003045.

[17] Yu C, Kim YS, Kim D, Grunlan JC. Thermoelectric behavior of segregated-network polymer nanocomposites. Nano Letters. 2008;8:4428–32. DOI: 10.1021/nl802345s.

[18] Du Y, Shen SZ, Cai K, Casey PS. Research progress on polymer–inorganic thermoelectric nanocomposite materials. Progress in Polymer Science. 2012;37:820–41. DOI: 10.1016/j.progpolymsci.2011.11.003.

[19] Wang L, Yao Q, Bi H, Huang F, Wang Q, Chen L. PANI/graphene nanocomposite films with high thermoelectric properties by enhanced molecular ordering. Journal of Materials Chemistry A. 2015;3:7086–92. DOI: 10.1039/C4TA06422D.

[20] Song H, Cai K, Wang J, Shen S. Influence of polymerization method on the thermoelectric properties of multi-walled carbon nanotubes/polypyrrole composites. Synthetic Metals. 2016;211:58–65. DOI: 10.1016/j.synthmet.2015.11.013.

[21] Lee W, Kang YH, Lee JY, Jang K-S, Cho SY. Improving the thermoelectric power factor of CNT/PEDOT: PSS nanocomposite films by ethylene glycol treatment. RSC Advances. 2016;6:53339–44. DOI: 10.1039/C6RA08599G.

[22] Gao C, Chen G. Conducting polymer/carbon particle thermoelectric composites: emerging green energy materials. Composites Science and Technology. 2016;124:52–70. DOI: 10.1016/j.compscitech.2016.01.014.

[23] Dey A, Bajpai OP, Sikder AK, Chattopadhyay S, Khan MAS. Recent advances in CNT/graphene based thermoelectric polymer nanocomposite: a proficient move towards waste energy harvesting. Renewable and Sustainable Energy Reviews. 2016;53:653–71. DOI: 10.1016/j.rser.2015.09.004.

[24] Qin F, Brosseau C. A review and analysis of microwave absorption in polymer composites filled with carbonaceous particles. Journal of Applied Physics. 2012;111:061301. DOI: 10.1063/1.3688435.

[25] Thostenson ET, Ren Z, Chou T-W. Advances in the science and technology of carbon nanotubes and their composites: a review. Composites Science and Technology. 2001;61:1899–912. DOI: 10.1016/S0266-3538(01)00094-X.

[26] Bauhofer W, Kovacs JZ. A review and analysis of electrical percolation in carbon nanotube polymer composites. Composites Science and Technology. 2009;69:1486–98. DOI: 10.1016/j.compscitech.2008.06.018.

[27] Iijima S. Helical microtubules of graphitic carbon. Nature. 1991;354:56–8. DOI: 10.1038/354056a0.

[28] Xie XL, Mai YW, Zhou XP. Dispersion and alignment of carbon nanotubes in polymer matrix: a review. Materials Science & Engineering R-Reports. 2005;49:89–112. DOI: 10.1016/j.mser.2005.04.002.

[29] BCC Research LLC. Global Markets and Technologies for Carbon Nanotubes [Internet]. 2012. Available from: www.bccreserach.com [Accessed: 2016-08-24].

[30] Latil S, Roche S, Mayou D, Charlier J-C. Mesoscopic transport in chemically doped carbon nanotubes. Physical Review Letters. 2004;92:256805. DOI: 10.1103/PhysRevLett.92.256805.

[31] Terrones M, Ajayan PM, Banhart F, Blase X, Carroll DL, Charlier JC, et al. N-doping and coalescence of carbon nanotubes: synthesis and electronic properties. Applied Physics a-Materials Science & Processing. 2002;74:355–61. DOI: 10.1007/s003390201278.

[32] Zhong DY, Liu S, Zhang GY, Wang EG. Large-scale well aligned carbon nitride nanotube films: low temperature growth and electron field emission. Journal of Applied Physics. 2001;89:5939–43. DOI: 10.1063/1.1370114.

[33] Sharifi T, Hu G, Jia XE, Wagberg T. Formation of active sites for oxygen reduction reactions by transformation of nitrogen functionalities in nitrogen-doped carbon nanotubes. ACS Nano. 2012;6:8904–12. DOI: 10.1021/nn302906r.

[34] Pels JR, Kapteijn F, Moulijn JA, Zhu Q, Thomas KM. Evolution of nitrogen functionalities in carbonaceous materials during pyrolysis. Carbon. 1995;33:1641–53. DOI: 10.1016/0008-6223(95)00154-6.

[35] Arjmand M, Sundararaj U. Effects of nitrogen doping on X-band dielectric properties of carbon nanotube/polymer nanocomposites. ACS Applied Materials & Interfaces. 2015;7:17844–50. DOI: 10.1021/acsami.5b04211.

[36] Kanygin MA, Sedelnikova OV, Asanov IP, Bulusheva LG, Okotrub AV, Kuzhir PP, et al. Effect of nitrogen doping on the electromagnetic properties of carbon nanotube-based composites. Journal of Applied Physics. 2013;113:144315. DOI: 10.1063/1.4800897.

[37] Arjmand M, Ameli A, Sundararaj U. Employing nitrogen doping as innovative technique to improve broadband dielectric properties of carbon nanotube/polymer nanocomposites. Macromolecular Materials and Engineering. 2016;301:555-65. DOI: 10.1002/mame.201500365.

[38] Krause B, Ritschel M, Täschner C, Oswald S, Gruner W, Leonhardt A, et al. Comparison of nanotubes produced by fixed bed and aerosol-CVD methods and their electrical percolation behaviour in melt mixed polyamide 6.6 composites. Composites Science and Technology. 2010;70:151–60. DOI: 10.1016/j.compscitech.2009.09.018.

[39] Arjmand M, Chizari K, Krause B, Pötschke P, Sundararaj U. Effect of synthesis catalyst on structure of nitrogen-doped carbon nanotubes and electrical conductivity and electromagnetic interference shielding of their polymeric nanocomposites. Carbon. 2016;98:358–72. DOI: 10.1016/j.carbon.2015.11.024.

[40] Ding F, Larsson P, Larsson JA, Ahuja R, Duan HM, Rosen A, et al. The importance of strong carbon-metal adhesion for catalytic nucleation of single-walled carbon nanotubes. Nano Letters. 2008;8:463–8. DOI: 10.1021/nl072431m.

[41] Chizari K, Vena A, Laureritius L, Sundararaj U. The effect of temperature on the morphology and chemical surface properties of nitrogen-doped carbon nanotubes. Carbon. 2014;68:369–79. DOI: 10.1016/j.carbon.2013.11.013.

[42] Yuan JK, Yao SH, Dang ZM, Sylvestre A, Genestoux M, Bai JB. Giant dielectric permittivity nanocomposites: realizing true potential of pristine carbon nanotubes in polyvinylidene fluoride matrix through an enhanced interfacial interaction. Journal of Physical Chemistry C. 2011;115:5515–21. DOI: 10.1021/jp1117163.

[43] Arjmand M, Sundararaj U. Impact of $BaTiO_3$ as insulative ferroelectric barrier on the broadband dielectric properties of MWCNT/PVDF nanocomposites. Polymer Composites. 2016;37:299–304. DOI: 10.1002/pc.23181.

[44] Dang ZM, Yao SH, Yuan JK, Bai JB. Tailored dielectric properties based on microstructure change in BaTiO(3)-carbon nanotube/polyvinylidene fluoride three-phase nanocomposites. Journal of Physical Chemistry C. 2010;114:13204–9. DOI: 10.1021/jp103411c.

[45] Krause B, Boldt R, Häußler L, Pötschke P. Ultralow percolation threshold in polyamide 6.6/MWCNT composites. Composites Science and Technology. 2015;114:119–25. DOI: 10.1016/j.compscitech.2015.03.014.

[46] Arjmand M, Sundararaj U. Electromagnetic interference shielding of nitrogen-doped and undoped carbon nanotube/polyvinylidene fluoride nanocomposites: a comparative study. Composites Science and Technology. 2015;118:257–63. DOI: 10.1016/j.compscitech.2015.09.012.

[47] Kaiser KL. Electromagnetic Shielding. Boca Raton: CRC Press; 2006. 336 p.

[48] Blythe T, Bloor D. Electrical Properties of Polymers. 2nd ed. New York: Cambridge University Press; 2005. 480 p.

[49] Weber M, Kamal MR. Estimation of the volume resistivity of electrically conductive composites. Polymer Composites. 1997;18:711–25. DOI: 10.1002/pc.10324.

[50] Arjmand M, Mahmoodi M, Gelves GA, Park S, Sundararaj U. Electrical and electromagnetic interference shielding properties of flow-induced oriented carbon nanotubes in polycarbonate. Carbon. 2011;49:3430–40. DOI: 10.1016/j.carbon.2011.04.039.

[51] Lux F. Models proposed to explain the electrical conductivity of mixtures made of conductive and insulating materials. Journal of Materials Science. 1993;28:285–301. DOI: 10.1007/bf00357799.

[52] Li J, Ma PC, Chow WS, To CK, Tang BZ, Kim JK. Correlations between percolation threshold, dispersion state, and aspect ratio of carbon nanotubes. Advanced Functional Materials. 2007;17:3207–15. DOI: 10.1002/adfm.200700065.

[53] Behnam A, Guo J, Ural A. Effects of nanotube alignment and measurement direction on percolation resistivity in single-walled carbon nanotube films. Journal of Applied Physics. 2007;102:044313. DOI: 10.1063/1.2769953.

[54] Arjmand M, Mahmoodi M, Park S, Sundararaj U. An innovative method to reduce the energy loss of conductive filler/polymer composites for charge storage applications. Composites Science and Technology. 2013;78:24–9. DOI: 10.1016/j.compscitech.2013.01.019.

[55] Arjmand M, Apperley T, Okoniewski M, Sundararaj U. Comparative study of electromagnetic interference shielding properties of injection molded versus compression molded multi-walled carbon nanotube/polystyrene composites. Carbon. 2012;50:5126–34. DOI: 10.1016/j.carbon.2012.06.053.

[56] Balberg I. Tunneling and nonuniversal conductivity in composite materials. Physical Review Letters. 1987;59:1305–8. DOI: 10.1103/PhysRevLett.59.1305.

[57] Sichel EK, Gittleman JI, Sheng P. Transport properties of the composite material carbon-poly(vinyl chloride). Physical Review B. 1978;18:5712–6. DOI: 10.1103/PhysRevB.18.5712.

[58] Li C, Thostenson ET, Chou T-W. Dominant role of tunneling resistance in the electrical conductivity of carbon nanotube–based composites. Applied Physics Letters. 2007;91:223114. DOI: 10.1063/1.2819690.

[59] Chekanov Y, Ohnogi R, Asai S, Sumita M. Electrical properties of epoxy resin filled with carbon fibers. Journal of Materials Science. 1999;34:5589–92. DOI: 10.1023/A:1004737217503.

[60] Spitalsky Z, Tasis D, Papagelis K, Galiotis C. Carbon nanotube-polymer composites: chemistry, processing, mechanical and electrical properties. Progress in Polymer Science. 2010;35:357–401. DOI: 10.1016/j.progpolymsci.2009.09.003.

[61] TabkhPaz M, Mahmoodi M, Arjmand M, Sundararaj U, Chu J, Park SS. Investigation of chaotic mixing for MWCNT/polymer composites. Macromolecular Materials and Engineering. 2015;300:482–96. DOI: 10.1002/mame.201400361.

[62] Thomassin J-M, Jérôme C, Pardoen T, Bailly C, Huynen I, Detrembleur C. Polymer/carbon based composites as electromagnetic interference (EMI) shielding materials. Materials Science and Engineering: R: Reports. 2013;74:211–32. DOI: 10.1016/j.mser.2013.06.001.

[63] Sharifi T, Nitze F, Barzegar HR, Tai CW, Mazurkiewicz M, Malolepszy A, et al. Nitrogen doped multi walled carbon nanotubes produced by CVD-correlating XPS and Raman

spectroscopy for the study of nitrogen inclusion. Carbon. 2012;50:3535–41. DOI: 10.1016/j.carbon.2012.03.022.

[64] Barzegar HR, Gracia-Espino E, Sharifi T, Nitze F, Wagberg T. Nitrogen doping mechanism in small diameter single-walled carbon nanotubes: impact on electronic properties and growth selectivity. Journal of Physical Chemistry C. 2013;117:25805–16. DOI: 10.1021/jp409518m.

[65] Moisala A, Nasibulin AG, Kauppinen EI. The role of metal nanoparticles in the catalytic production of single-walled carbon nanotubes—a review. Journal of Physics-Condensed Matter. 2003;15:S3011–35. DOI: 10.1088/0953-8984/15/42/003.

[66] Nasibulin AG, Altman IS, Kauppinen EI. Semiempirical dynamic phase diagrams of nanocrystalline products during copper (II) acetylacetonate vapour decomposition. Chemical Physics Letters. 2003;367:771–7. DOI: 10.1016/s0009-2614(02)01795-5.

[67] Alvarez WE, Kitiyanan B, Borgna A, Resasco DE. Synergism of Co and Mo in the catalytic production of single-wall carbon nanotubes by decomposition of CO. Carbon. 2001;39:547–58. DOI: 10.1016/s0008-6223(00)00173-1.

[68] Huang Y, Li N, Ma YF, Feng D, Li FF, He XB, et al. The influence of single-walled carbon nanotube structure on the electromagnetic interference shielding efficiency of its epoxy composites. Carbon. 2007;45:1614–21. DOI: 10.1016/j.carbon.2007.04.016.

[69] Singh BP, Saini K, Choudhary V, Teotia S, Pande S, Saini P, et al. Effect of length of carbon nanotubes on electromagnetic interference shielding and mechanical properties of their reinforced epoxy composites. Journal of Nanoparticle Research. 2013;16:2161. DOI: 10.1007/s11051-013-2161-9.

[70] Maciel IO, Anderson N, Pimenta MA, Hartschuh A, Qian HH, Terrones M, et al. Electron and phonon renormalization near charged defects in carbon nanotubes. Nature Materials. 2008;7:878–83. DOI: 10.1038/nmat2296.

[71] Rao AM, Richter E, Bandow S, Chase B, Eklund PC, Williams KA, et al. Diameter-selective Raman scattering from vibrational modes in carbon nanotubes. Science. 1997;275:187–91. DOI: 10.1126/science.275.5297.187.

[72] Dresselhaus MS, Dresselhaus G, Jorio A, Souza AG, Saito R. Raman spectroscopy on isolated single wall carbon nanotubes. Carbon. 2002;40:2043–61. DOI: 10.1016/s0008-6223(02)00066-0.

[73] Picher M, Anglaret E, Arenal R, Jourdain V. Processes controlling the diameter distribution of single-walled carbon nanotubes during catalytic chemical vapor deposition. ACS Nano. 2011;5:2118–25. DOI: 10.1021/nn1033086.

[74] Villalpando-Paez F, Zamudio A, Elias AL, Son H, Barros EB, Chou SG, et al. Synthesis and characterization of long strands of nitrogen-doped single-walled carbon

nanotubes. Chemical Physics Letters. 2006;424:345–52. DOI: 10.1016/j.cplett.2006.04.074.

[75] Ibrahim EMM, Khavrus VO, Leonhardt A, Hampel S, Oswald S, Rummeli MH, et al. Synthesis, characterization, and electrical properties of nitrogen-doped single-walled carbon nanotubes with different nitrogen content. Diamond and Related Materials. 2010;19:1199–206. DOI: 10.1016/j.diamond.2010.05.008.

[76] Ramesh BP, Blau WJ, Tyagi PK, Misra DS, Ali N, Gracio J, et al. Thermogravimetric analysis of cobalt-filled carbon nanotubes deposited by chemical vapour deposition. Thin Solid Films. 2006;494:128–32. DOI: 10.1016/j.tsf.2005.08.220.

[77] Khalkhal F, Carreau PJ, Ausias G. Effect of flow history on linear viscoelastic properties and the evolution of the structure of multiwalled carbon nanotube suspensions in an epoxy. Journal of Rheology (1978-present). 2011;55:153–75. DOI: 10.1122/1.3523628.

[78] Khalkhal F, Carreau PJ. Scaling behavior of the elastic properties of non-dilute MWCNT–epoxy suspensions. Rheologica Acta. 2011;50:717–28. DOI: 10.1007/s00397-010-0527-9.

[79] Ureña-Benavides EE, Kayatin MJ, Davis VA. Dispersion and rheology of multiwalled carbon nanotubes in unsaturated polyester resin. Macromolecules. 2013;46:1642–50. DOI: 10.1021/ma3017844.

[80] Xiao JR, Gama BA, Gillespie JW. An analytical molecular structural mechanics model for the mechanical properties of carbon nanotubes. International Journal of Solids and Structures. 2005;42:3075–92. DOI: 10.1016/j.ijsolstr.2004.10.031.

[81] Ewoldt RH, Winter P, Maxey J, McKinley GH. Large amplitude oscillatory shear of pseudoplastic and elastoviscoplastic materials. Rheologica Acta. 2010;49:191–212. DOI: 10.1007/s00397-009-0403-7.

[82] Hyun K, Wilhelm M, Klein CO, Cho KS, Nam JG, Ahn KH, et al. A review of nonlinear oscillatory shear tests: analysis and application of large amplitude oscillatory shear (LAOS). Progress in Polymer Science. 2011;36:1697–753. DOI: 10.1016/j.progpolymsci.2011.02.002.

[83] Ewoldt RH, Hosoi AE, McKinley GH. New measures for characterizing nonlinear viscoelasticity in large amplitude oscillatory shear. Journal of Rheology. 2008;52:1427. DOI: 10.1122/1.2970095.

[84] Sprakel J, Lindström SB, Kodger TE, Weitz DA. Stress enhancement in the delayed yielding of colloidal gels. Physical Review Letters. 2011;106:248303. DOI: 10.1103/PhysRevLett.106.248303.

[85] Sadeghi S, Zehtab Yazdi A, Sundararaj U. Controlling short-range interactions by tuning surface chemistry in HDPE/graphene nanoribbon nanocomposites. The Journal of Physical Chemistry B. 2015;119:11867–78. DOI: 10.1021/acs.jpcb.5b03558.

[86] Pham KN, Petekidis G, Vlassopoulos D, Egelhaaf SU, Pusey PN, Poon WCK. Yielding of colloidal glasses. EPL (Europhysics Letters). 2006;75:624. DOI: 10.1209/epl/i2006-10156-y.

[87] Laurati M, Egelhaaf S, Petekidis G. Nonlinear rheology of colloidal gels with intermediate volume fraction. Journal of Rheology (1978-present). 2011;55:673–706. DOI: 10.1122/1.3571554.